The Astrophysical Journal, 856:179 (14pp), 2018 April 1 https://doi.org/10.3847/1538-4357/aab614

Three-dimensional MHD Simulations of Solar Prominence Oscillations in a Magnetic Flux Rope

Yu-Hao Zhou[1,2,3], C. Xia[4], R. Keppens[2], C. Fang[1,3], and P. F. Chen[1,3]
[1] School of Astronomy and Space Science, Nanjing University, Nanjing 210023, People's Republic of China; chenpf@nju.edu.cn
[2] Centre for mathematical Plasma Astrophysics, Department of Mathematics, KU Leuven, Celestijnenlaan 200B, B-3001 Leuven, Belgium; chun.xia@ynu.edu.cn
[3] Key Laboratory of Modern Astronomy & Astrophysics (Nanjing University), Ministry of Education, Nanjing 210023, People's Republic of China
[4] School of Physics and Astronomy, Yunnan University, Kunming 650050, People's Republic of China
Received 2018 February 6; revised 2018 March 7; accepted 2018 March 8; published 2018 April 5

Abstract

Solar prominences are subject to all kinds of perturbations during their lifetime, and frequently demonstrate oscillations. The study of prominence oscillations provides an alternative way to investigate their internal magnetic and thermal structures because the characteristics of the oscillations depend on their interplay with the solar corona. Prominence oscillations can be classified into longitudinal and transverse types. We perform three-dimensional ideal magnetohydrodynamic simulations of prominence oscillations along a magnetic flux rope, with the aim of comparing the oscillation periods with those predicted by various simplified models and examining the restoring force. We find that the longitudinal oscillation has a period of about 49 minutes, which is in accordance with the pendulum model where the field-aligned component of gravity serves as the restoring force. In contrast, the horizontal transverse oscillation has a period of about 10 minutes and the vertical transverse oscillation has a period of about 14 minutes, and both of them can be nicely fitted with a two-dimensional slab model. We also find that the magnetic tension force dominates most of the time in transverse oscillations, except for the first minute when magnetic pressure overwhelms it.

Key words: magnetohydrodynamics (MHD) – methods: numerical – Sun: filaments, prominences – Sun: oscillations

1. Introduction

Magnetic field plays an important role in the heating and all kinds of dynamics of the solar atmosphere. However, the magnetic field in the corona can hardly be measured directly. Luckily, bodily oscillations of coronal structures such as coronal loops (Aschwanden et al. 1999; Nakariakov et al. 1999) and solar filaments (Tripathi et al. 2009) open a new window to diagnose the corona. Solar filaments, called prominences when observed above the solar limb (the two terminologies are used interchangeably in this paper), are cold dense plasma magnetically suspended in the corona. Their oscillations can provide some clues from which to infer the local magnetic structure (Arregui et al. 2012). Compared with coronal loops, oscillations of the solar prominences have been studied more extensively since the discovery of winking filaments (Dodson 1949; Hyder 1966; Ramsey & Smith 1966; Kleczek & Kuperus 1969). Ramsey & Smith (1966) analyzed several oscillating filaments, and one of them oscillates four times, being triggered by four different flares. The fact that the periods are the same in the four episodes indicates that the oscillation period is determined by the intrinsic properties of the filament, regardless of the origin of the trigger.

Prominence oscillations can be classified in different ways. Early on, they were classified into short- and long-period oscillations, with the periods being $\leqslant$10 minutes (e.g., Tsubaki & Takeuchi 1986) for the former and $\geqslant$40 minutes for the latter (e.g., Bashkirtsev et al. 1983; Bashkirtsev & Mashnich 1984). It is noted that oscillations with short and long periods can co-exist in one prominence (Bocchialini et al. 2011). Recent studies have usually classified them according to their velocity amplitudes into small-amplitude oscillations ($\sim$2–3 km s^{-1}; see Oliver & Ballester 2002; Oliver 2009; Arregui et al. 2012, for a review) and large-amplitude oscillations ($\geqslant$20 km s^{-1}; see Tripathi et al. 2009, for a review). Another widely used classification is based on the oscillation direction relative to the magnetic field. In this case, prominence oscillations can be divided into longitudinal oscillations, whose direction of motion is parallel to the local magnetic field inferred from the filament threads, and transverse oscillations, where the displacements are perpendicular to the filament threads. On average, longitudinal oscillations show a longer period than transverse oscillations. This kind of classification might be more physical since it seems that longitudinal and transverse oscillations have their own individual restoring forces, which are the crucial factor for oscillations. However, it should be emphasized here that it is not straightforward to distinguish the longitudinal and transverse modes: whether an oscillation is longitudinal or transverse is determined by the oscillation direction relative to the local magnetic field (or filament threads) rather than to the filament spine. Since the filament threads are skewed from the filament spine with an angle from several degrees to 30° (Athay et al. 1983; Hanaoka & Sakurai 2017), longitudinal oscillations would also manifest transverse displacement relative to the filament spine in Hα images (Pant et al. 2015; Chen et al. 2017). Note that the transverse oscillations can be further divided into horizontal ones (Isobe & Tripathi 2006; Asai et al. 2012; Gosain & Foullon 2012; Shen et al. 2014) and vertical ones (Eto et al. 2002; Okamoto et al. 2004; Gilbert et al. 2008).

Transverse oscillations of prominences with a typical period of 10–20 minutes have been investigated theoretically since the 1960s. In early studies, Hyder (1966) and Kleczek & Kuperus (1969) approximated an oscillating prominence as a single mass harmonic oscillator, with the magnetic tension force being the restoring force. Later the prominence was modeled as a dense cold slab embedded in the hot tenuous corona along a

magnetic flux tube (see Joarder & Roberts 1992, for an example), where the slab has a finite length but infinite width and height. In such a slab model, the global oscillation of the prominence is described by the string model, with the oscillation period determined by

$$P = 2\pi (WL)^{1/2}/v, \quad (1)$$

where L is the half-length of the flux tube, W is the half-length of the prominence, while v represents a typical fast, slow, or Alfvén speed in the prominence. Following these pioneering explorations, more complicated models for transverse oscillations were proposed. In these models, more observational facts are considered, such as gravity (Oliver et al. 1993), the angle between the prominence and magnetic lines (Joarder & Roberts 1993), the prominence–corona transition region (PCTR, Oliver & Ballester 1996), the finite transverse extent of the prominence (Díaz et al. 2001, 2002), non-adiabatic effects (Terradas et al. 2001), mass flows (Soler et al. 2008), ion–neutral collisions (Soler et al. 2010), and so on (see Arregui et al. 2012, for a review). It is noticed that the increased complexity usually fails to allow a simple analytical solution. Moreover, the magnetic flux tube that supports the prominence has a three-dimensional (3D) nature with strong curvature. As a result, the vertical and horizontal transverse oscillations might display significant differences. However, in various simplified models, horizontal and vertical transverse oscillations are identical. All these features can be better captured with 3D magnetohydrodynamic (MHD) simulations, and the results in the above-mentioned analytical models can be examined or verified with 3D MHD simulations.

Longitudinal oscillations were discovered only 15 years ago (Jing et al. 2003). Since then, many cases have been reported (Jing et al. 2006; Vršnak et al. 2007; Li & Zhang 2012; Zhang et al. 2012, 2017; Luna et al. 2014; Shen et al. 2014). Oscillations of this type have a period of the order of 1 hr, several times longer than that of typical transverse oscillations. Jing et al. (2003) proposed several mechanisms for the restoring force to explain the longitudinal oscillations of filaments, such as field-aligned gravity and pressure enhancement due to an Alfvén wave package bouncing back and forth along the anchored magnetic loop. They also considered the possibility that the observed longitudinal oscillations might be an apparent motion due to successive transverse oscillations of neighboring threads of the filament. Vršnak et al. (2007) suggested the magnetic pressure gradient to be the restoring force of the longitudinal oscillations, where the increase in magnetic pressure was thought to result from the injection of poloidal magnetic flux into the filament via magnetic reconnection. In their model, an expression for the oscillation period P was derived as $P \approx 4.4L/v_{A\phi}$, where L is the half-length of the magnetic flux rope and $v_{A\phi}$ is the Alfvén speed based on the equilibrium poloidal field of the filament.

Later, more effort was devoted to the field-aligned component of gravity as the restoring force. For example, Luna & Karpen (2012) proposed the "pendulum model" to explain the filament longitudinal oscillations, where the field-aligned component of gravity serves as the restoring force for the filament threads to oscillate along the magnetic dips. With an analogy to the pendulum, the oscillation period is determined by the curvature radius (R) of the magnetic dip, i.e., $P = 2\pi\sqrt{R/g}$, where g is the solar gravitational acceleration near the solar surface. More convincingly, Zhang et al. (2012) compared one-dimensional (1D) radiative hydrodynamic numerical simulations with observations of prominence longitudinal oscillations. In the setup of their simulation, the geometry of the magnetic dip, which determines the curvature radius R, was taken from observations. It turned out that the oscillation period in the simulation is consistent with the observations. Since they found in their simulations that the gravity component overwhelms the gas pressure gradient, their results strongly favor the field-aligned component of gravity as the restoring force for filament longitudinal oscillations. They further performed a parameter survey on how the oscillation period and decay time depend on the geometry of the magnetic configuration (Zhang et al. 2013).

Terradas et al. (2013) extended the simulations into two dimensions (2D) by numerically solving the linearized MHD equations. However, they found that the oscillation period is 2–3 times longer than that predicted by the pendulum model. Regarding this discrepancy, Luna et al. (2016) pointed out that the inconsistency is due to the fact that the filament in Terradas et al. (2013) is supported by magnetic flux tubes with dips that are too shallow. If the magnetic dips are too shallow, the field-aligned component of gravity no longer overwhelms the gas pressure gradient. When the filament is located in deeper magnetic dips, further simulations indicate that the oscillation period becomes consistent with the pendulum model again. So far, the filament longitudinal oscillations have been simulated in 1D and 2D only, where the magnetic configuration is markedly simplified. To have a more realistic magnetic configuration, we need to resort to 3D MHD simulations.

In this paper, we aim to perform 3D MHD simulations of both longitudinal and transverse oscillations of solar filaments. Our paper is organized as follows. The setup of our simulation and the numerical method are described in Section 2. The numerical results of the simulations are presented in Section 3, which is followed by discussions in Section 4.

2. Numerical Method

Prominence oscillations are observed in both active-region prominences and quiescent prominences, and we know that active-region prominences usually have a stronger magnetic field than quiescent prominences. Since a strong magnetic field implies the need for more computational resources, a model representing quiescent prominences is selected for our simulation. Statistical analysis reveals that ~96% of the quiescent prominences are supported by a magnetic flux rope (Ouyang et al. 2017). Therefore, a flux rope is adopted as the magnetic structure for our simulations.

Our basic setup is similar to Xia & Keppens (2016). We start from a static coronal volume in a Cartesian box. The extent of the box is -180 Mm $< x <$ 180 Mm, -120 Mm $< y <$ 120 Mm, and $0 < z <$ 240 Mm. The number density starts from 10^9 cm^{-3} at the bottom boundary and decreases exponentially to satisfy hydrostatic equilibrium in a 1 MK isothermal corona. In order to obtain a force-free magnetic field, we prescribe the following distribution of the z-component of the magnetic field in a plane below our bottom boundary at $z = -4$ Mm, where

the z-axis is upward:

$$B_z(x, y) = \begin{cases} 0 & y < -\delta_y; \\ B_{z0}\sin(\pi y/\delta_y)\exp(x_m^2/\delta_x^2) & -\delta_y \leqslant y \leqslant \delta_y; \\ 0 & y > \delta_y. \end{cases} \quad (2)$$

Here $x_m = \mathrm{minmod}(x + x_0, x - x_0)$ is the median of $x + x_0$, $x - x_0$, and 0. The parameters in Equation (2) are chosen as follows: $B_{z0} = 25$ G, $\delta_x = 30$ Mm, $\delta_y = 80$ Mm, and $x_0 = 50$ Mm. The bipolar magnetogram described by Equation (2) is placed below our bottom boundary in order to avoid any sharp variation of magnetic field resulting from the extrapolation. The force-free parameter α in our extrapolation is chosen to be a constant, -0.08. The resulting plasma β ranges from 0.015 to 0.5 for $z < 100$ Mm, and goes up to about 1.4 near the top boundary.

In order to form a magnetic flux rope from the above-mentioned force-free field, we first perform simulations by solving the following isothermal MHD equations:

$$\frac{\partial \rho}{\partial t} + \nabla \cdot (\rho \boldsymbol{v}) = 0, \quad (3)$$

$$\frac{\partial (\rho \boldsymbol{v})}{\partial t} + \nabla \cdot \left(\rho \boldsymbol{v}\boldsymbol{v} + p_{\mathrm{tot}} \boldsymbol{I} - \frac{\boldsymbol{B}\boldsymbol{B}}{\mu_0} \right) = \rho \boldsymbol{g}, \quad (4)$$

$$\frac{\partial \boldsymbol{B}}{\partial t} + \nabla \cdot (\boldsymbol{v}\boldsymbol{B} - \boldsymbol{B}\boldsymbol{v}) = 0, \quad (5)$$

where $p_{\mathrm{tot}} = p + B^2/2\mu_0$ is the total pressure, $\boldsymbol{g} = -g_\odot r_\odot^2/(r_\odot + z)^2 \hat{\boldsymbol{e}}_z$ is the gravitational acceleration, $g_\odot = 274\ \mathrm{m\,s^{-2}}$ is the gravitational acceleration at the solar surface, and $r_\odot = 691$ Mm is the solar radius. All the other symbols in the equations have their usual meanings. The evolution is driven by a surface flow that is described as follows:

$$\begin{cases} v_x(x, y) = f(t) C (\partial |B_{mz}|/\partial y) \exp(-y^2/\delta_y^2) \\ \qquad\qquad \times [\mathrm{sgn}(y + \delta_y/2) - \mathrm{sgn}(y - \delta_y/2)]; \\ v_y(x, y) = -v_x(x, y); \\ v_z(x, y) = 0, \end{cases} \quad (6)$$

where t is the time and $f(t)$ is a linear ramp function allowing us to progressively change the driving velocity according to

$$f(t) = \begin{cases} t/t_{\mathrm{ramp}} & 0 \leqslant t < t_{\mathrm{ramp}}; \\ 1 & t_{\mathrm{ramp}} \leqslant t \leqslant t_{\mathrm{max}} - t_{\mathrm{ramp}}; \\ (t_{\mathrm{max}} - t)/t_{\mathrm{ramp}} & t_{\mathrm{max}} - t_{\mathrm{ramp}} < t \leqslant t_{\mathrm{max}}. \end{cases} \quad (7)$$

In our simulation, t_{ramp} and t_{max} are 14.3 minutes and 100.2 minutes, respectively. The parameter C is used to control the maximum value of our driving velocity to be 12.8 km s^{-1}, which is larger than observational values but still much smaller than the Alfvén speed in the corona.

The normal component of the magnetic field at the boundaries is derived from the inner points in order to keep the field divergence-free (in a centered difference scheme). For other variables at the four lateral boundaries, a zero-gradient extrapolation is applied. At the bottom boundary, density is fixed to keep the gravitational stratification. At the top boundary, we extrapolate the velocity and adopt a gravitationally stratified density profile.

Equations (3)–(5) are solved numerically using the adaptive mesh refinement (AMR) versatile advection code (MPI-AMRVAC; Keppens et al. 2012; Porth et al. 2014; Xia et al. 2018). A four-level AMR grid is used, whose base grid level is $144 \times 96 \times 96$, and it will reach an effective resolving power of 312 km $\times$ 312 km $\times$ 312 km at the finest cells. As shown in Figure 1(a)–(e), after imposing the driving flow, the magnetic field becomes more and more sheared. After about 50 minutes, a small flux rope is formed, and then it grows while rising slightly. Then, after another 50 minutes when the driving flow is completely stopped, we get a large elongated flux rope. This flux rope has a length of about 200 Mm in the x-direction with a cross-sectional diameter of about 40 Mm. The center of the flux rope is located at a height of about 35 Mm from the bottom boundary, and the maximum magnetic field strength is about 16 G.

However, we found that the flux rope formed in this way is not force-free enough. Therefore, at the end of this stage, a magneto-frictional method is imposed for 60,000 iteration steps (see Guo et al. 2016, for details of this method used in MPI-AMRVAC). Figure 1(f) shows the magnetic field lines we eventually got. While apparently the configuration does not change too much compared to Figure 1(e), actually the maximum current density is reduced by half, which implies that the magnetic field becomes smoother. For prominence longitudinal oscillations, the magnetic field we then obtain is fairly weak, so that also transverse oscillations would be easily excited. In order to avoid such mode coupling, we multiply the magnetic field by a factor of 1.5 for the simulation of longitudinal oscillations. Since each component of the magnetic field is amplified by the same factor, the resulting magnetic field is force-free as well.

So far, we have obtained a hydrostatic isothermal atmosphere and an almost force-free magnetic field with a 3D flux rope embedded in an envelope field. As the final step to get our initial setup for prominence oscillations, we follow Xia & Keppens (2016) and replace the isothermal atmosphere with an idealized chromosphere and corona, whose temperature distribution is expressed as follows:

$$T(z) = \begin{cases} T_{\mathrm{ch}} + (T_{\mathrm{co}} - T_{\mathrm{ch}})(1 + \tanh(z - h_{\mathrm{tr}} - c_1)/w_{\mathrm{tr}})/2 \\ \qquad z \leqslant h_{\mathrm{tr}}, \\ (7F_c(z - h_{\mathrm{tr}})/(2\kappa) + T_{\mathrm{tr}}^{7/2})^{2/7} \qquad z > h_{\mathrm{tr}}, \end{cases} \quad (8)$$

where $h_{\mathrm{tr}} = 4$ Mm is the height of our "transition region." The transition region is slightly higher than in reality (see also Hillier & van Ballegooijen 2013; Hansteen et al. 2017). We take $T_{\mathrm{ch}} = 1.5 \times 10^4$ K, $T_{\mathrm{tr}} = 1.6 \times 10^5$ K, and $T_{\mathrm{co}} = 1.5 \times 10^6$ K, which are typical values for the temperatures of the chromosphere, the transition region, and the corona, respectively. $F_c = 2 \times 10^5\ \mathrm{erg\,cm^{-2}\,s^{-1}}$ is the constant vertical thermal conduction flux and $\kappa = 10^{-6} T^{5/2}\ \mathrm{erg\,cm^{-1}\,s^{-1}\,K^{-1}}$ is the *Spitzer*-type heat conductivity. Then, we use a hyperbolic tangent function with parameters $c_1 = 0.333$ Mm and $w_{\mathrm{tr}} = 0.3$ Mm to extend the temperature profile from the corona into the chromosphere. The resulting temperature ranges from 1.5×10^4 K at the bottom boundary to about 2.3×10^6 K near the top boundary. By assuming a hydrostatic atmosphere, we then derive the density distribution ρ_{old}, starting from a given number density of $8.33 \times 10^{12}\ \mathrm{cm^{-3}}$ at the bottom.

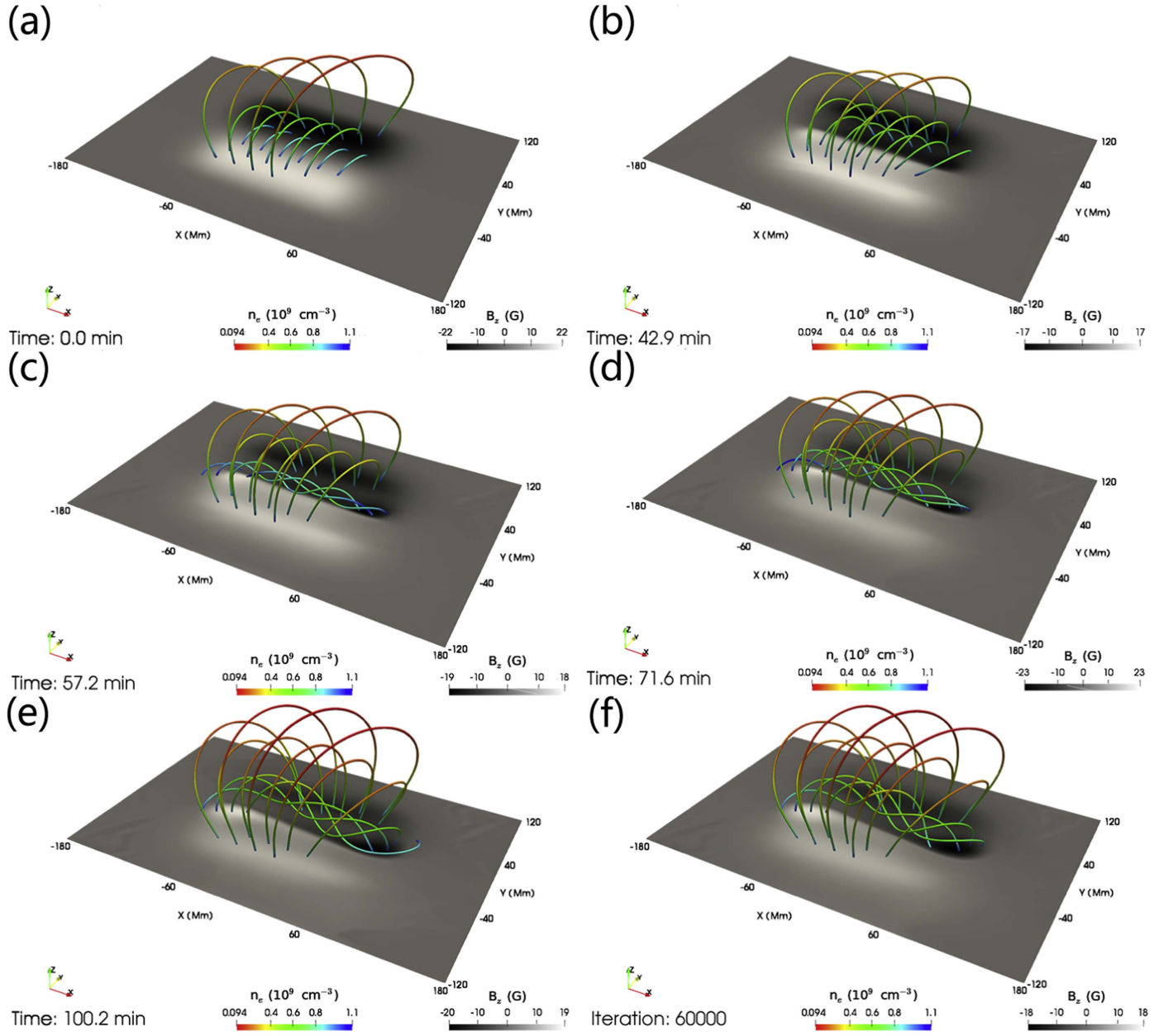

Figure 1. (a)–(e) Five moments of the magnetic field evolving from a sheared arcade to an elongated flux rope. The field lines are colored by number density. The grayscale in the bottom plane indicates the evolving z-component of the magnetic field. (f) The magnetic field we get after the magneto-frictional relaxation.

The next step is to construct a model prominence. This can be done by performing simulations of the evaporation–condensation (Xia & Keppens 2016) or reconnection–condensation models (Kaneko & Yokoyama 2017), which are computationally expensive. Since we do not focus on the physical process of prominence formation, we choose here to build a prominence in a more convenient way simply by increasing the density by about two orders of magnitude while keeping the gas pressure unchanged, as done by Terradas et al. (2015) and Zhou et al. (2017). Following other authors (e.g., Terradas et al. 2016) and guided by our own experience, we choose to build the prominence by modifying the density distribution from $\rho_{\rm old}$ to $\rho_{\rm new}$, which is expressed as

$$\rho_{\rm new}=\begin{cases}\rho_{\rm old}\left[1+C_\rho\left(1+\tanh\left(\dfrac{l_x-|x|}{w_x}\right)\right)\left(1+\tanh\left(\dfrac{l_y-|y|}{w_y}\right)\right)\left(1+\tanh\left(\dfrac{l_z-|z-z_0(x)|}{w_z}\right)\right)\right] & |x|<l_x;\\ \rho_{\rm old}\left[1+C_\rho\left(1+\tanh\left(\dfrac{l_y-|y|}{w_y}\right)\right)\left(1+\tanh\left(\dfrac{l_z-|z-z_0(x)|}{w_z}\right)\right)\right] & |x|\geqslant l_x,\end{cases} \tag{9}$$

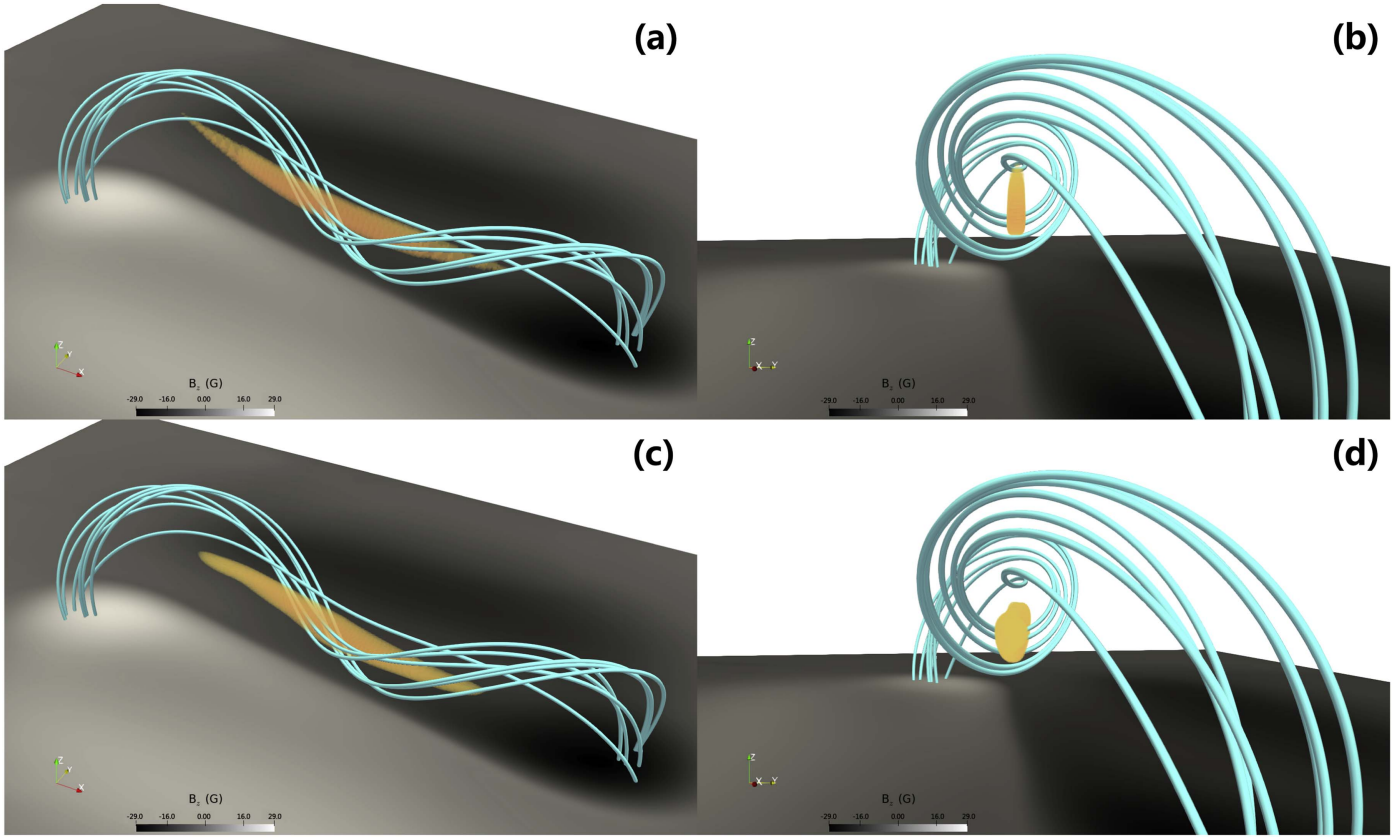

Figure 2. (a), (b) Two perspectives of the prominence inserted into a force-free magnetic field. (c), (d) Two perspectives of the prominence and the 3D magnetic field lines when the inserted prominence reaches its final equilibrium. In this figure, the yellow isosurface traces the prominence layer whose density is 20 times the background density, and the light blue lines are selected magnetic field lines enveloping the prominence. The grayscale in the bottom plane indicates the z-component of the magnetic field.

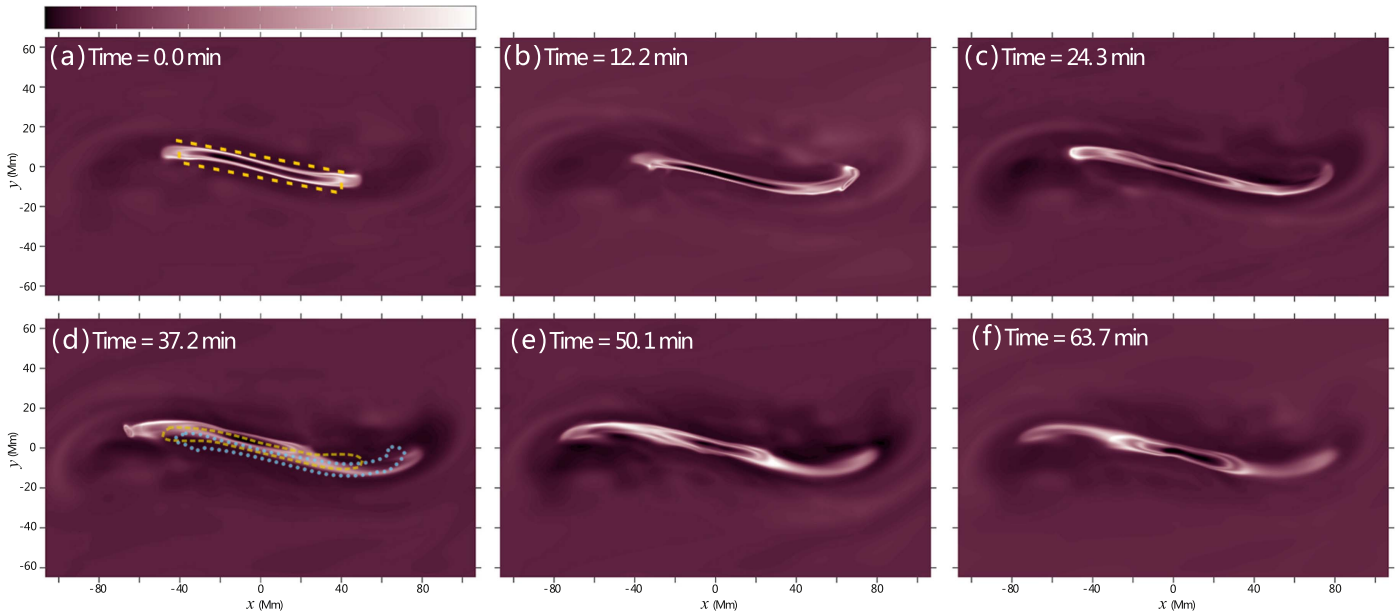

Figure 3. Top view of the synthesized EUV 211 Å images of the longitudinally oscillating filament at six moments. The parallelogram in panel (a) marks the slice used for plotting Figure 4, and the yellow dashed line and the cyan dotted line in panel (d) mark the initial and the rightmost positions of the filament.

where $l_x = 7.5$ Mm, $l_y = 1.5$ Mm, $l_z = 4$ Mm, $w_x = 35$ Mm, $w_y = 0.3$ Mm, and $w_z = 0.8$ Mm. $C_\rho = 12.5$ is a parameter used to control the density contrast with the background corona. The parameter $z_0(x) = 20 + z_c - \sqrt{\max(z_c^2 - x^2, 0)}$ Mm is the initial height of the prominence centroid, where $z_c = 100$ Mm. Then, we rotate the density distribution by an angle of 10° with respect to the z-axis by multiplying the density array with a rotation matrix, which aligns the prominence with the flux rope.

With these operations the prominence has a maximum density 44.4 times the background one, and a temperature of 1.4×10^4 K. Figures 2(a) and (b) show the inserted prominence and the magnetic field lines viewed in two different perspectives, where the yellow isosurface traces the prominence layer whose density is 20 times the background density, and the light blue lines represent the magnetic structure enveloping the prominence. The approximate volume of the prominence is about 70 Mm × 5 Mm × 10 Mm with a total mass of 4.7×10^{10} kg, which is a typical value for a light prominence similar to previous work (Terradas et al. 2015, 2016). It is noted that the inserted state is not in equilibrium. Therefore, we allow the whole system to evolve for about half an hour until the maximum velocity within the prominence is less than $2\,\mathrm{km\,s^{-1}}$, which is one order of magnitude smaller than the perturbation velocity used for prominence oscillations. The relaxed state of the prominence and the field lines viewed from two perspectives are displayed in Figures 2(c) and (d), where the prominence is suspended at a height of 18.5 Mm for the case of longitudinal oscillations. We use the relaxed state as the real initial conditions for our numerical simulations in this paper.

It is also mentioned that, from this stage on, the full ideal MHD equations are solved numerically, which means we also solve the internal energy equation

$$\frac{\partial e_{\rm int}}{\partial t} + \nabla \cdot (e_{\rm int}\boldsymbol{v}) = -p\nabla \cdot \boldsymbol{v}, \tag{10}$$

where $e_{\rm int} = p/(\gamma - 1)$ is the internal energy. The heat capacity ratio $\gamma = 5/3$ represents an adiabatic process.

3. Perturbations and Oscillations

In order to study filament oscillations, velocity perturbations are imposed on the prominence. Different directions of the velocity lead to longitudinal, horizontal transverse, and vertical transverse oscillations. Taking the longitudinal oscillations as an example, the perturbation velocity we impose here is

$$(x, y, z) = v_1(x, y, z)\frac{B(x, y, z)}{|B(x, y, z)|}, \tag{11}$$

where v_1 is in a form similar to Equation (9), i.e.,

$$\begin{aligned} v_1(x, y, z) = v_0 &\left(1 + \tanh\left(\frac{l_{vx} - |x|}{w_{vx}}\right)\right) \\ &\times \left(1 + \tanh\left(\frac{l_{vy} - |y|}{w_{vy}}\right)\right) \\ &\times \left(1 + \tanh\left(\frac{l_{vz} - |z - z_{v0}|}{w_{vz}}\right)\right). \end{aligned} \tag{12}$$

The parameters in Equation (12) are chosen as follows so that the perturbation region is larger than the prominence while much smaller than our simulation box: $l_{vx} = 100$ Mm, $l_{vy} = 50$ Mm, $l_{vz} = 4$ Mm, $w_{vx} = 30$ Mm, $w_{vy} = 15$ Mm, and $w_{vz} = 10$ Mm. The height $z_{v0} = 18$ Mm is a little lower than z_0 in Equation (9) since the height of the prominence decreases a little after the relaxation step. v_0 is a constant used to control the maximum velocity perturbation. For transverse oscillations, we just change the direction of the velocity perturbation in Equation (11), making it orthogonal to the magnetic field instead. We actually considered three methods to excite global filament oscillations in the simulations. One is to specify the velocity perturbation in and around the filament. The second is to add a high-pressure region next to the filament to mimic thermal energy released by nearby magnetic reconnection. The third is to introduce a shock wave, which is possibly induced by a remote coronal mass ejection, and let the shock impact the filament. As demonstrated by Zhang et al. (2013), the oscillation characteristics are nearly the same under impulsive high-pressure and direct velocity perturbation. Therefore, we take the first method and include large-scale perturbations only in the filament, excluding secondary effects by an external perturbation on the filament environment. This is numerically convenient and representative for anything that results in bulk movement of a filament.

3.1. Longitudinal Oscillations

To trigger a longitudinal oscillation, we simply impose a velocity perturbation described by Equation (11) on the filament. The velocity is aligned with the magnetic field lines with a maximum value of $25\,\mathrm{km\,s^{-1}}$ and decreases gradually down to zero in its neighborhood. To compare our results with observations more clearly, synthesized emission in the extreme ultraviolet (EUV) waveband at 211 Å is calculated from the simulation data. The emission in each cell of our domain is calculated via

$$I_\lambda(x, y, z) = G_\lambda(T)n_e^2(x, y, z), \tag{13}$$

where the wavelength $\lambda = 211$ Å and G_λ is the temperature-dependent response function for the 211 Å waveband, which is obtained directly from the CHIANTI atomic database (Dere et al. 1997; Del Zanna et al. 2015). Figure 3 shows a time sequence of the 211 Å images of our results from a top view. The emission is integrated along the line of sight, in this case the z-direction. For simplicity, we suppose that the emissions from the chromosphere are uniform and invariant. Thus, they are ignored in the integral. It is seen that, as the longitudinal velocity perturbation is exerted, the filament starts to move to the right. At $t = 12.2$ minutes, it reaches its furthest location and starts to bounce back (Figure 3(b)). The filament returns to its original position at about $t = 24.3$ minutes and continues to move to the left (Figure 3(c)). It reaches its leftmost position at $t = 37.2$ minutes (Figure 3(d)). At $t = 50.1$ minutes, the filament finishes its first cycle of oscillation (Figure 3(e)) and starts to repeat. However, as revealed by Figure 3(f), the amplitude of the oscillation becomes smaller and smaller, i.e., the oscillation gradually decays. To see the motion more clearly, in Figure 3(d) we overplot the initial boundary of the filament as the yellow dashed line whereas its rightmost position is the cyan dotted line. It is noticed that during the oscillation, the filament material spreads out to form a more diffuse structure than the initial state.

In order to display the longitudinal oscillation more clearly, we trace the density distribution along the main axis of the filament. The axis is taken to be parallel to the x–y plane at $z = 18.5$ Mm, and is skewed from the x-axis by 10° in order to be aligned with the filament. Since the motion is not exactly along this selected axis, the axis has a width of 5 Mm in the y-direction, as marked by the yellow parallelogram in Figure 3(a). The evolution of the integrated density distribution

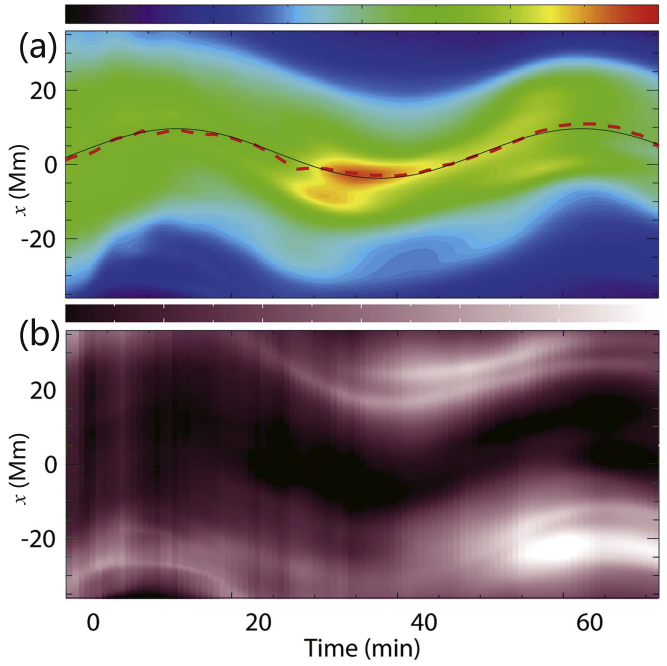

Figure 4. Time–distance diagram of the integrated density along the selected axis with a width of 5 Mm (see Figure 3(a)). The red dashed line indicates the position of the filament centroid, whereas the black solid line is the fitting result based on a decayed sine function. (b) Synthesized EUV 211 Å image of panel (a).

along the main axis is plotted in the time–distance diagram in Figure 4. It reveals that the filament experiences a decayed oscillation. We further calculate the centroids of the dense plasma along the main axis at individual times, which are represented by the red dashed line in Figure 4. The positions of these centroids are then fit with a decayed sinusoidal function $d = d_0 e^{-t/\tau} \sin(2\pi t/P + \phi)$, where d is the displacement of the filament, d_0 is the amplitude, P is the oscillation period, τ is the decay time, and ϕ is the initial phase angle. The fitting results in an oscillation period of $P = 48.8$ minutes and a decay time $\tau = 86.5$ minutes. The fitted profile is overplotted on Figure 4 as the black solid line. The corresponding 211 Å image is plotted in Figure 4(b) for comparison.

3.2. Horizontal Transverse Oscillations

By changing the perturbation velocity from Equation (11) to $v_x = v_1 \min(B_y, 0)/|\boldsymbol{B}|$ and $v_y = v_1 B_x/|\boldsymbol{B}|$, we can excite the horizontal transverse oscillation of the filament.

The evolution of the synthesized EUV 171 Å images viewed from the top is displayed in Figure 5. Similarly, the emission from the chromosphere is not included in the calculation of the EUV intensity. From the figure, it is seen that at $t = 3.2$ minutes, the filament reaches its furthest position in the positive y-direction (Figure 5(b)), and starts to return to the original location. At $t = 8.2$ minutes, the filament moves to its furthest position in the negative y-direction, as indicated by Figure 5(c). The filament returns to its equilibrium position at $t = 10.7$ minutes. After that, it repeats its oscillation, but with a smaller amplitude, as revealed by Figure 5(d). Similarly to the longitudinal oscillation, the initial and the uppermost positions of the prominence boundary are respectively indicated by the cyan dashed line and the blue dotted line in Figure 5(c).

In order to show the lateral displacement more clearly, we take a slice across the filament in the y-direction at $z = 18.0$ Mm, as indicated by the cyan dashed line in Figure 5(a). The evolution of density along the slice is displayed in the time–distance diagram in Figure 6, where the red dashed line describes the evolution of the prominence centroid. Its displacement is fit with a decayed sinusoidal function $d = d_0 e^{-t/\tau} \sin(2\pi t/P + \phi)$, which leads to a period of 10.1 minutes and a decay time $\tau = 17.5$ minutes. The fitting is shown by the black solid line. The corresponding 171 Å image is plotted in Figure 6(b) for comparison.

3.3. Vertical Transverse Oscillations

Once the perturbation velocity in Equation (11) is modified to $\boldsymbol{v}_{\rm per}(x, y, z) = v_1(x, y, z)\hat{\boldsymbol{e}}_z$, we can excite vertical transverse oscillations. Although the direction of velocity is not exactly perpendicular to the magnetic field lines, the deviation is minor since the magnetic field is nearly horizontal inside the prominence.

Again, synthesized 171 Å images are used to show the dynamics of the filament viewed from the side, i.e., the y-direction. The results are displayed in Figure 7, where the chromosphere is colored in white since it does not change too much, and its features would distract the attention of the reader. It is seen that at $t = 3.6$ minutes, as revealed by Figure 7(b), the prominence goes down to its lowest height (Figure 7(c)) and then starts to bounce back. At $t = 11.1$ minutes, the prominence reaches its highest position. The prominence reaches its minimum height again at $t = 17.9$ minutes, as shown in Figure 7(d). Again, the initial and the lowest positions of the prominence are respectively indicated by the cyan dashed line and the navy blue dotted line in Figure 7(c). Comparing panels (d) and (b), we can see that the amplitude of the oscillation is decaying.

In order to reveal the vertical oscillation more quantitatively, we examine the density distribution along the z-axis, which crosses the center of the prominence. The slice is marked by the cyan dashed line in Figure 7(a). The evolution of the density distribution along the z-axis is displayed in the time–distance diagram in Figure 8, from which the decayed oscillation is evident. The center of mass of the prominence is represented by the dashed line, and the evolution of position is fit with a decayed sine function $z = z_0 + A_0 e^{-t/\tau} \sin(2\pi t/P + \phi)$, where z_0 is the initial height, A_0 is the initial amplitude of the oscillation, P is the period, τ is the decay time, and ϕ is the initial phase angle. The resulting period is 14.0 minutes. The corresponding 171 Å image is plotted in Figure 8(b) for comparison.

4. Discussions

Prominence oscillations are a very interesting phenomenon. They can not only be applied as a potential precursor for coronal mass ejections (Chen et al. 2008; Parenti 2014; Mashnich & Bashkirtsev 2016; Zhou et al. 2016), but can also be used to diagnose the coronal magnetic field (Arregui et al. 2012). As a part of coronal seismology (Nakariakov & Verwichte 2005; Andries et al. 2009), prominence seismology seems more complicated than its coronal loop counterpart due to the complex structure of the former. Among all the parameters obtained from observations, oscillation periods and damping time are two straightforward quantities that can be used to constrain the restoring force and the damping mechanisms. Many linear models have been established for

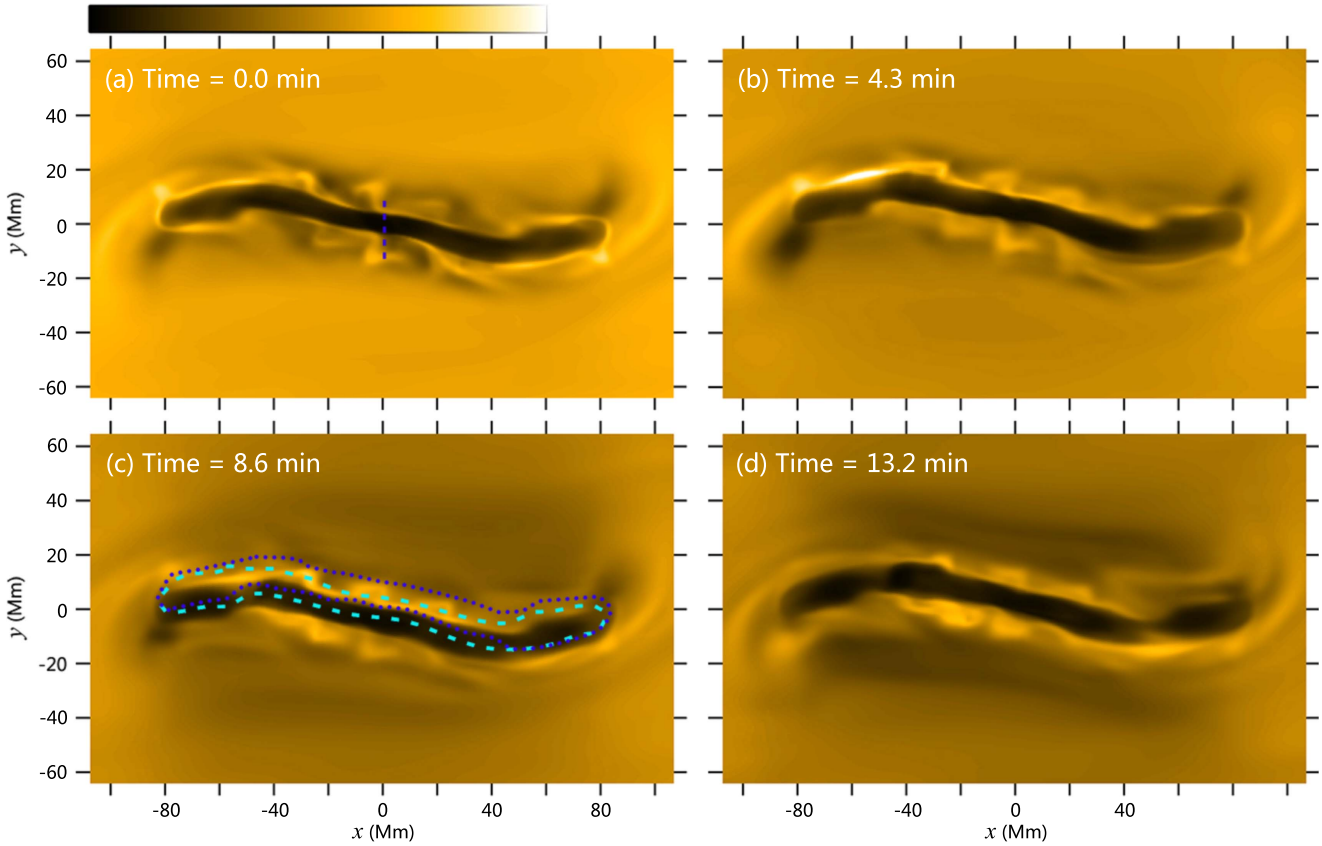

Figure 5. Top view of the synthesized EUV 171 Å images at four moments in the case where the filament is experiencing horizontal transverse oscillations. The cyan dashed line and the blue dotted line in panel (c) indicate the initial and the uppermost positions of the prominence, respectively.

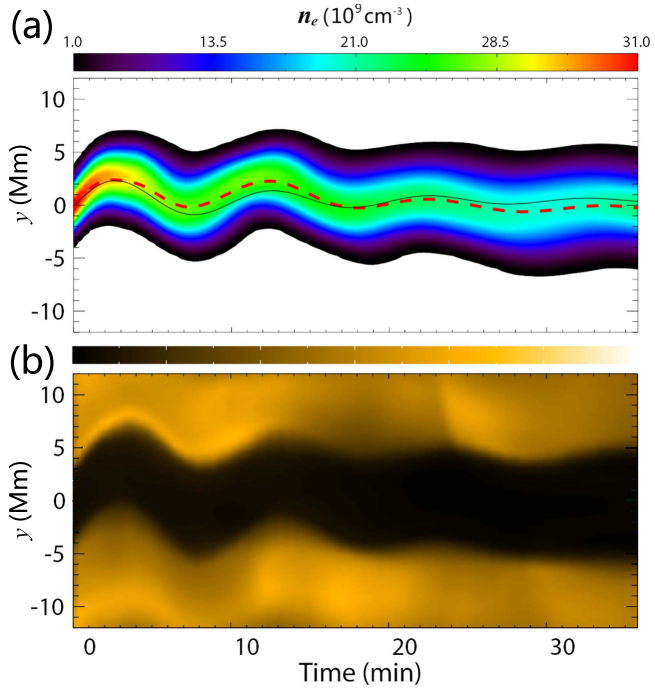

Figure 6. Time–distance diagram of the density along the *y*-axis (taken along the blue dashed line in Figure 5(a)). The red dashed line indicates the position of the filament centroid, whereas the black solid line is the fitting result based on a decayed sine function. (b) The synthesized EUV 171 Å image of panel (a).

different restoring forces (Oliver & Ballester 2002) and damping mechanisms (Oliver 2009), and the validity of these linear models should be verified by nonlinear MHD simulations. In this paper, we performed 3D MHD simulations of prominence oscillations, and concentrated on the restoring forces only, leaving the damping mechanism for future work. Investigating the damping mechanisms requires a much higher spatial resolution in the numerical simulations for the physical processes to stand out from the numerical dissipation.

To obtain a model prominence embedded in a magnetic flux rope, we first created a nearly force-free flux rope via evolving the bottom boundary conditions in an isothermal MHD simulation. Then, the density was increased and the temperature was decreased inside an ellipsoidal volume. Such distributions, which are not in mechanical equilibrium, gradually evolved to an equilibrium state through relaxation. We must be aware of some artifacts of this model prominence due to our ideal MHD assumptions. For example, looking at Equation (9), we may find that we set a fairly large PCTR in the spine direction, which may not be true in observations. Then we imposed an impulsive perturbation over the prominence, which could be due to a passing EUV wave (Shen et al. 2014). The direction of the perturbation was controlled in order to excite longitudinal, horizontal transverse, and vertical transverse oscillations.

4.1. Pendulum Model for the Longitudinal Oscillations

As shown by Figure 4, our numerical results indicate that the centroid of the prominence oscillates with a period of about 48.8 minutes, which is in the typical range for the observed longitudinal oscillations (Tripathi et al. 2009). In order to check the pendulum model, we extract the magnetic field line across the prominence centroid, and calculate the curvature radius

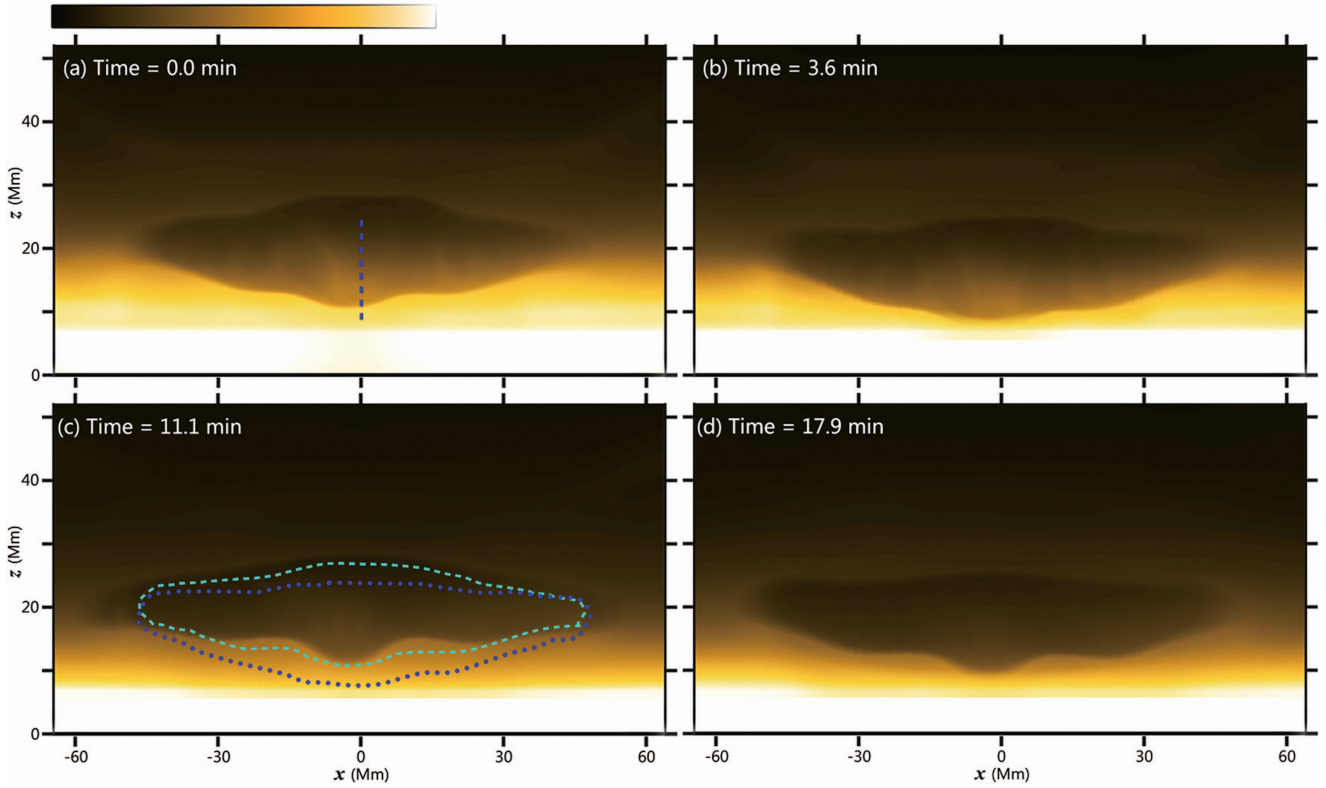

Figure 7. Side view of the synthesized EUV 171 Å images at four moments in the case where the filament is experiencing vertical transverse oscillations. The cyan dashed line and the blue dotted line in panel (c) indicate the initial and the extremal positions of the prominence, respectively.

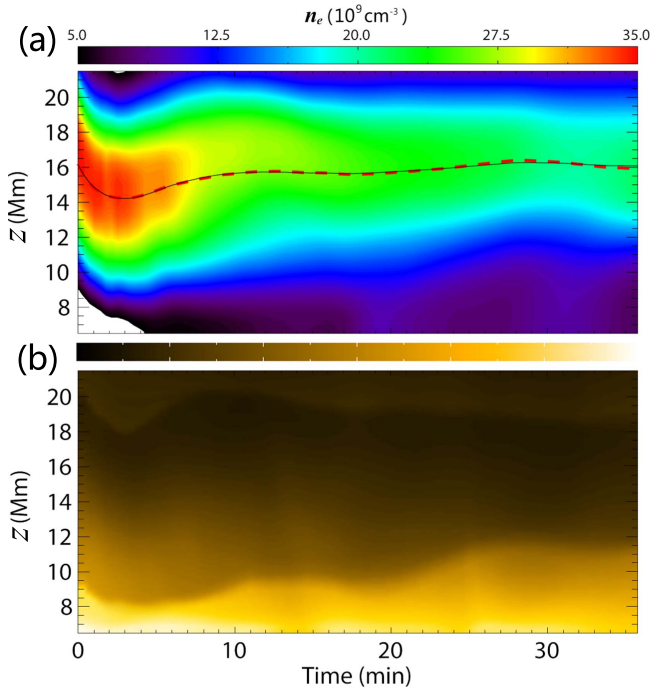

Figure 8. Time–distance diagram of the density along the z-axis. The red dashed line indicates the position of the prominence centroid, whereas the black solid line is the fitting result based on a decayed sine function. (b) The synthesized EUV 171 Å image of panel (a).

near the magnetic dip, which is found to be $R = 52.6$ Mm. According to the pendulum model, the theoretical period of the longitudinal oscillation should be $P = 2\pi\sqrt{R/g} = 45.9$ minutes, which is very close to the oscillation period in our 3D MHD simulations. Such consistency confirms that the field-aligned component of gravity is responsible for the restoring force for filament longitudinal oscillations.

On the other hand, as mentioned by Terradas et al. (2013), different parts of the prominence at different heights may not oscillate in phase. They oscillate with different periods. In order to check this, 10 field lines passing through the z-axis at $t = 0$ are selected, from heights between $z = 12$ Mm and $z = 21$ Mm, with a separation of 1 Mm. Following the analysis in Luna et al. (2016), the density-weighted average field-aligned velocity is calculated as

$$v_{\parallel i}(t) = \int v_{\parallel}(s_i, t)\rho(s_i, t)ds_i \Big/ \int \rho(s_i, t)ds_i, \qquad (14)$$

where i means the ith field line we select and s_i is the 1D arc length along the field line. Here, the velocity, instead of the displacement, is considered because the magnetic lines themselves are also moving. The results are plotted in Figure 9(a), where the x-axis is the physical time in minutes. Ten profiles with different colors are stacked one by one in the sequence of height, and the zero velocity for each profile is indicated by the dashed line with the same color as the corresponding velocity profile. Each profile is fit with a decayed sine function, and the resulting periods, as a function of height of the magnetic dip, are plotted as solid circles in Figure 9(b). It is seen that the oscillation period increases from 43 to 59 minutes as the height of the plasma increases. According to the pendulum model, such a result means that the curvature radius of the magnetic dips becomes larger and larger at higher positions. To confirm this, we calculate the curvature radius (R) for each magnetic field line at the dip site in our

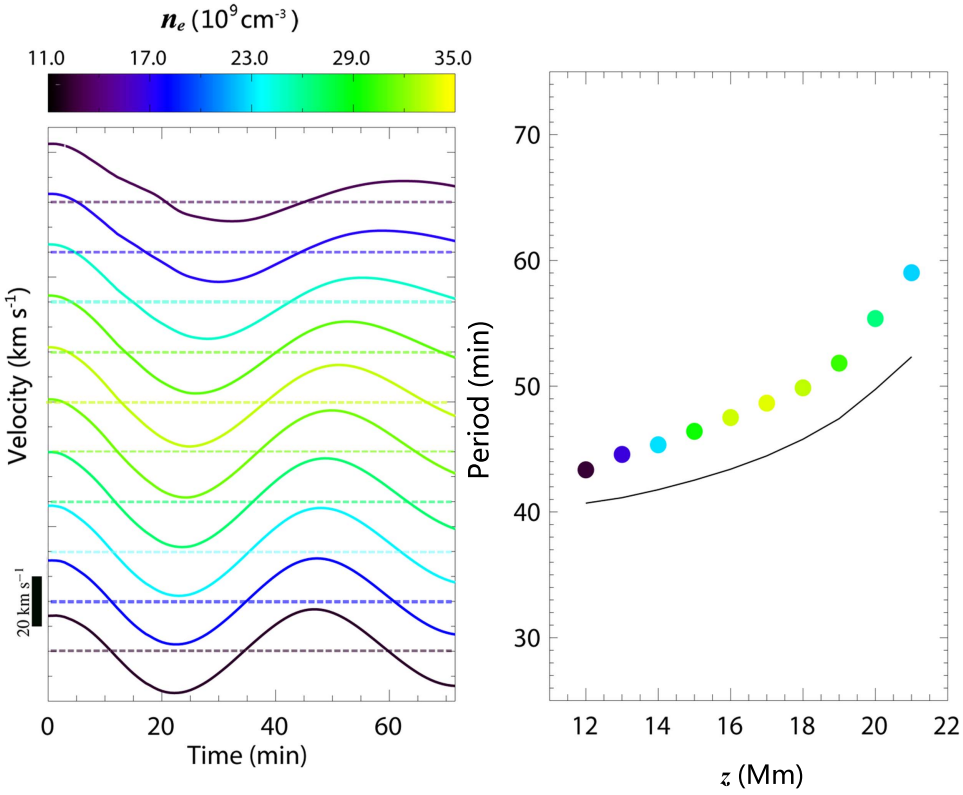

Figure 9. Left panel: evolution of the density-weighted average field-aligned velocity of 10 selected magnetic field lines in the case of longitudinal oscillation. The horizontal axis is physical time and the velocity profiles of different field lines are stacked one by one in the sequence of their heights. The scale for the velocity is plotted at the lower left corner. Different colors indicate different initial densities at the center of the magnetic dips of different field lines, and the color scale for the density is shown at the top of this panel. Right panel: oscillation periods of the 10 selected magnetic field lines at different heights, where the solid circles are derived from our simulations, and the black solid line represents the theoretical values calculated from the pendulum model. The color of each circle has the same meaning as in panel (a), indicating the averaged density along the field line.

numerical results. It is noted that the magnetic dip is not a perfect circle. Therefore, we take an average value within ± 10 Mm near the center of the magnetic dip, assuming that the magnetic field lines do not deform during the oscillations. Indeed it is found that the curvature radius of the magnetic dips increases with height. Based on the pendulum model, i.e., $P = 2\pi\sqrt{R/g}$, the theoretical periods of the longitudinal oscillations along these field lines are calculated and plotted as the solid line in Figure 9(b). We can see that the theoretical results are roughly in agreement with the numerical results, further confirming that the field-aligned component of gravity serves as the restoring force for filament longitudinal oscillations. However, it is noticed in Figure 9(b) that the theoretical results are systematically smaller than the 3D numerical results. The deviation is about 10%.

Two conditions are required for the pendulum model to work well: (1) the curvature radius of the magnetic dip should not be too large; and (2) the magnetic field line does not deform significantly during prominence oscillations. For the first requirement, Luna & Karpen (2012) introduced a reference radius of curvature, $R_{\rm lim}$ in their Equation (33). When the curvature radius of a magnetic dip, R, is smaller than $R_{\rm lim}$, the field-aligned component of gravity overwhelms the gas pressure gradient, and the gas pressure can be neglected. In our simulation, $R_{\rm lim}$ is about 450 Mm, and the curvature radius of the magnetic dips is $\sim$50 Mm, several times smaller than this. In our previous 1D simulations (Zhang et al. 2013; Zhou et al. 2017), the curvature radius of the magnetic dips was also smaller than $R_{\rm lim}$, which is why both the 3D simulations in this paper and our previous simulations showed consistency with the pendulum model. Regarding the second requirement, it is often argued that the plasma β should be much smaller than unity. Observations indicate that the magnetic field strength of a quiescent prominence is generally 10–30 G (Bommier et al. 1994; Merenda et al. 2006). The corresponding plasma $\beta = 0.05\frac{n}{10^{11}\,\mathrm{cm}^{-3}}\frac{T}{10^4\,\mathrm{K}}\left(\frac{B}{10\,\mathrm{G}}\right)^{-2}$ would be much smaller than unity for the typical density and temperature. In our simulation case, the plasma β inside the prominence is $\sim$0.01, much smaller than unity. Therefore, it seems that the two requirements are both satisfied.

While the simulation results are quite consistent with the pendulum model, it is still worthwhile to mention that the actual period of the longitudinal oscillations in our 3D simulations is systematically larger than that predicted by the pendulum model. This feature cannot be explained by the additional effect of gas pressure, because the inclusion of extra gas pressure gradient would increase the restoring force and hence shorten the oscillation period. For example, Luna & Karpen (2012) considered the combination of gravity and gas pressure. They found that the resulting oscillation period is smaller than that determined by gravity only. The possible reason for the larger period in simulations is the deformation of the magnetic field line (Li & Zhang 2012), which changes the local curvature radius dynamically. Whether the magnetic field can be deformed is not determined by the plasma β alone. We

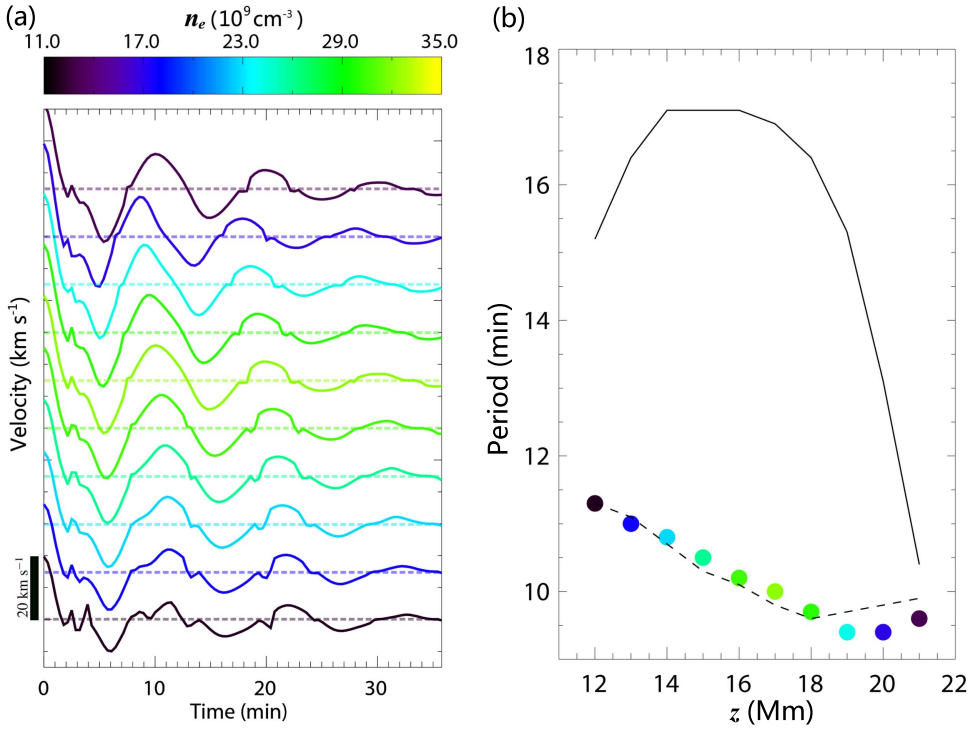

Figure 10. Similar to Figure 9, but for the y-component of velocity in the case of horizontal transverse oscillation. Two models are compared to the simulations on the right: a 2D slab model matches best.

think that another parameter should be the ratio of the gravity to the magnetic pressure

$$\delta = \frac{\rho g L}{B^2/2\mu_0} = 11.5 \frac{n}{10^{11}\ \mathrm{cm}^{-3}} \frac{L}{100\ \mathrm{Mm}} \left(\frac{B}{10\ \mathrm{G}}\right)^{-2}, \quad (15)$$

where n is the number density of the prominence, L is the length of the prominence thread, and B is the magnetic field. For the typical values of these parameters in our simulation, the newly defined dimensionless parameter δ is around unity, i.e., the gravity is comparable with the magnetic pressure force. Therefore, the deformation of the magnetic field lines is not negligible. The gravity-induced deformation makes the magnetic dip flatter, which increases the oscillation period.

4.2. Explanation for the Horizontal Transverse Oscillation

Our numerical results show that the horizontal transverse oscillation has a period of 9.9 ± 0.4 minutes. If we use the simple 1D string model, the oscillation period defined by Equation (1) (Joarder & Roberts 1992) is about 17 minutes, which is over 60% longer than the actual period. The reason for the discrepancy is that the prominence was assumed to be infinitely wide in their 1D model. While considering the finite width of prominences, Díaz et al. (2001) improved the 2D model of Joarder et al. (1997) and derived the new dispersion relation. Even for the fundamental mode of this model, the new equations become transcendental so that no analytic solution can be given, and the equations have to be solved numerically. The most important parameter required for this model, other than those needed for Equation (1), is the thickness of the prominence in the transverse direction, which can also be obtained directly from our simulation. Other parameters needed for this model, such as the density contrast, can also be obtained through averaging, though this model is not very sensitive to them. It is noted that the Alfvén speed used in this model is not taken inside the prominence, but outside it. Therefore, we take an average value of the Alfvén speed along the magnetic line in the corona, excluding the prominence part. The resulting oscillation period is ∼10 minutes, which is very close to our numerical simulation.

Similarly to the case of longitudinal oscillation, we also pick 10 different magnetic lines that pass through the z-axis at $t = 0$, and plot the time evolution of their density-weighted horizontal transverse velocity in Figure 10(a), where the zero velocity for each velocity profile is indicated by the dashed line with the corresponding color. The horizontal transverse oscillation presents a much shorter period than the longitudinal oscillation, which is in accordance with observations (Tripathi et al. 2009). Their oscillation periods can also be obtained by fitting the velocity profiles with decayed sine functions. However, since there are more fluctuations in the velocity profiles, we perform wavelet spectral analysis on the velocity evolutions, and the resulting period as a function of the height of the magnetic dip is displayed as solid circles in Figure 10(b). It is seen that, in contrast to the longitudinal case, the oscillation period decreases slightly with height.

The above-mentioned two linear models are compared with our simulation results. For the 1D string model, with all the parameters required for Equation (1) extracted from the simulations, the resulting periods for the 10 magnetic field lines are plotted as the solid line in Figure 10(b). It is seen that the theoretical periods deviate from the 3D simulation results significantly. For the 2D slab model (Díaz et al. 2001), with all the parameters in each magnetic field line included, the calculated oscillation periods are overplotted in Figure 10(b) as the dashed line. We can see that the 2D slab model matches the 3D simulation remarkedly well.

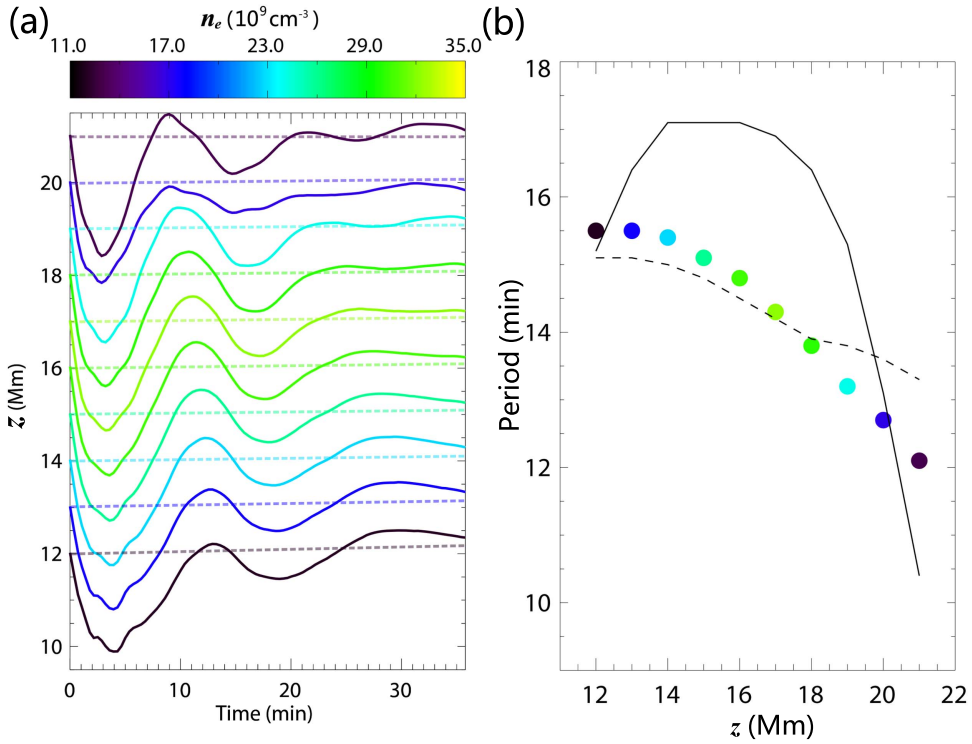

Figure 11. Similar to Figure 9, but for the displacement of the magnetic field lines in the z-direction in the case of vertical transverse oscillation.

It should be mentioned that the horizontal transverse oscillation periods of different parts of the prominence are not much different. It seems that the prominence oscillates horizontally as a whole.

4.3. Explanation for the Vertical Transverse Oscillation

The numerical results indicate that the vertical transverse oscillation of the prominence centroid has a period of 14.1 ± 1.5 minutes. If we use the simple 1D string model, the oscillation period defined by Equation (1) (Joarder & Roberts 1992) is about 17 minutes, which is ~20% larger than the actual period, which seems not so bad. It is noted here that the vertical and horizontal transverse oscillations are not distinguishable in the 1D string model. If we use the 2D slab model (Díaz et al. 2001), however, the calculated oscillation period is 14 minutes, which is almost the same as our 3D numerical simulations.

In order to check whether different parts of the prominence oscillate synchronously in the vertical transverse case, we select the same 10 magnetic lines as before to analyze their motions in detail. Different from the previous two subsections, for the vertical transverse oscillation we simply plot the displacements of these field lines in the z-direction because the magnetic lines near the prominence are almost horizontal, and the vertical displacement reflects the motion directly. The time evolutions of their displacements are plotted in Figure 11(a) as solid lines with different colors, where the equilibrium location for each line is indicated by the dashes with the corresponding color. We can see that the vertical motions in Figure 11(a) are much smoother than the horizontal transverse ones in Figure 10(a). Therefore, it is easy to fit these lines with decayed sine functions. The resulting period as a function of the height of the magnetic dip is displayed as solid circles in Figure 11(b). It is seen that the oscillation period decreases with height, with the same tendency as the horizontal transverse oscillation, but more drastically. Actually the difference in oscillation period among the 10 field lines is evident even by directly looking at the velocity profiles in Figure 11(a). It seems that the prominence is not oscillating collectively.

The two linear models are compared with our simulation results in this case as well. For the 1D string model, with all the parameters of each field line required for Equation (1) extracted from the simulations, the resulting periods for the 10 magnetic field lines are plotted as the solid line in Figure 11(b). It is seen that the theoretical periods deviate from the 3D simulation results significantly for most field lines. For the 2D slab model (Díaz et al. 2001), with all the parameters in each magnetic field line included (note that the vertical thickness of the prominence is the same for all the field lines), the calculated oscillation periods are overplotted in Figure 11(b) as the dashed line. We can see that the 2D slab model matches the 3D simulation better.

It is noted that, as seen from Figure 11(a), all the magnetic field lines have a tendency to rise slightly in altitude during oscillation. This is because some of the cold prominence material (about 20% of the total mass) drains down to the solar surface while oscillating vertically. The reduced gravity leads to the slow rise of the prominence. Another prominent feature of the vertical transverse oscillation, compared to the horizontal transverse oscillation, is that the two modes have different oscillation periods. The satisfactory matching between the 2D slab model and the 3D simulations implies that the difference in the oscillation period is simply due to the horizontal width being different from the vertical thickness of the prominence. In our case, the vertical thickness of the prominence is about three times larger than the horizontal width. In this sense, it seems that the effect of the curvature of the 3D magnetic field lines is negligible. Such a characteristic was also valid for

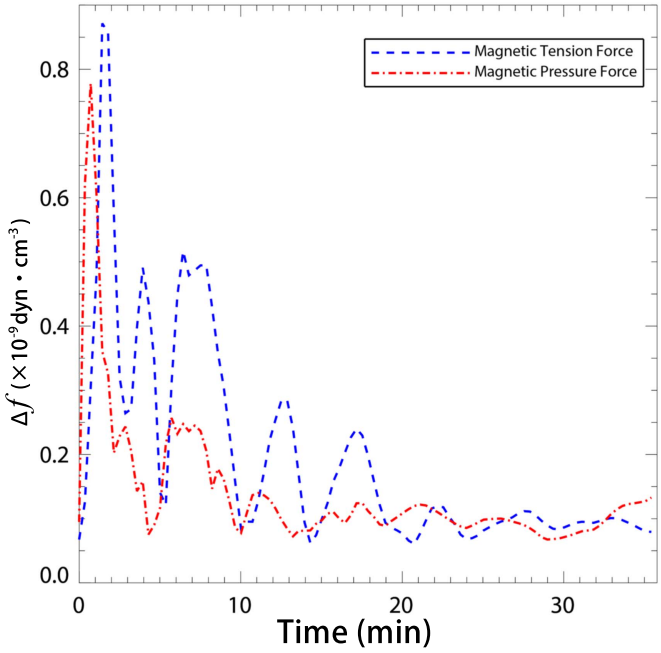

Figure 12. Time evolution of the normalized magnetic tension force and magnetic pressure force averaged along a selected magnetic field line. The magnetic tension is seen to dominate in the restoring force during most of the oscillation.

coronal loop oscillations (van Doorsselaere et al. 2009; Terradas et al. 2016). It is also inferred that when the horizontal and vertical transverse oscillations are observed to have similar periods (e.g., Ning et al. 2009), this probably implies that the aspect ratio of the cross section of the prominence is close to unity.

4.4. Restoring Force for the Transverse Oscillations

It is conceivable that the restoring force for the transverse oscillations is the Lorentz force, i.e., $\boldsymbol{J} \times \boldsymbol{B}$, which can be decomposed into the magnetic pressure force and the magnetic tension force as follows:

$$\boldsymbol{J} \times \boldsymbol{B} = -\nabla(B^2/2\mu_0) + \frac{\boldsymbol{B} \cdot \nabla \boldsymbol{B}}{\mu_0}, \tag{16}$$

where the first term on the right is the magnetic pressure force and the second term is the magnetic tension force. To investigate which term is dominant in the case of the horizontal transverse oscillation, we select a magnetic line that passes through the z-axis at $z = 17$ Mm when $t = 0$, and calculate the horizontal components of the Lorentz force, the tension force, and the magnetic pressure force along this field line. Then, we define the averaged change of the magnetic tension force and the magnetic pressure force weighted by the deviation of the Lorentz force from the initial state as follows:

$$\Delta f(t) = \frac{\int |f(t) - f(0)||f_{\rm L}(t) - f_{\rm L}(0)|ds}{\int |f_{\rm L}(t) - f_{\rm L}(0)|ds}, \tag{17}$$

where f stands for the magnetic tension force or the magnetic pressure force, and $f_{\rm L}$ stands for the Lorentz force. The time evolution of Δf is plotted in Figure 12, where the blue line corresponds to the magnetic tension force and the red line represents the magnetic pressure force. It is revealed that the magnetic pressure force dominates for the first minute only, and the magnetic tension force becomes dominant thereafter. It is interesting to notice the periodic variations of both the normalized unsigned magnetic tension and the magnetic pressure force. The dominant tension force shows a period of ~5 minutes (except for the second peak), which is exactly half the filament oscillation period, as expected. The subordinate magnetic pressure force shows higher-frequency fluctuations in addition to the ~5 minute oscillation. The higher-frequency oscillations might be due to other oscillation modes, such as the sausage mode. Although the magnetic pressure force is not important for the consideration of the restoring force in this paper, its multi-period oscillations definitely deserve further investigations. We also did the same analysis for the vertical transverse oscillations, and found that the result is similar: only during the first minute is the magnetic pressure dominant. Thereafter, the magnetic tension force is always dominant during oscillations. Therefore, it is reasonable to assume that the magnetic tension force is the restoring force for the period analysis as used widely in the literature (see Arregui et al. 2012, for a review).

To summarize, we performed 3D MHD numerical simulations of prominence oscillations, including the longitudinal one and the transverse ones (both horizontal and vertical), with the purpose of comparing their oscillation periods with various models and examining their restoring forces. It is confirmed that the magnetic field-aligned component of gravity is responsible for longitudinal oscillation, and the magnetic tension force is the main restoring force for transverse oscillation. Whereas the oscillation period of the longitudinal oscillation can be determined by the pendulum model, with an error up to 20% for the shallowest dips present in our modeled flux rope, the period of the transverse oscillation can be nicely determined by the 2D slab model described by Díaz et al. (2001), where the width (or thickness) of the prominence in the oscillation direction is also an important parameter.

It should be noted here that the model prominence in our simulation is a monolithic body. However, prominences are observed to be composed of many thin threads (Lin 2011), and these threads might oscillate with the same period (Lin 2004) or different periods (Mashnich et al. 2009a, 2009b). The thread–thread interactions have been investigated in 1D (Zhou et al. 2017) by simulations and in 2D via linear analysis (Díaz & Roberts 2006), and deserve 3D simulations in future work.

P.F.C. was supported by the Chinese foundation (NSFC 11533005) and Jiangsu 333 Project (No. BRA2017359). Y.Z. was supported by China Scholarship Council under file No. 201606190134. Y.Z. acknowledges Ileyk El Mellah, Jannis Teunissen, Dimitrios Millas, Tong Shi, Yi-Kang Wang, Kai Yang, and Jie Hong for their help. C.X. thanks FWO (Research Foundation Flanders) for the award of postdoctoral fellowship. R.K. was supported by FWO and by KU Leuven Project (No. GOA/2015-014) and by the Interuniversity Attraction Poles Programme of the Belgian Science Policy Office (IAP P7/08 CHARM). The simulations were conducted on the VSC (Flemish Supercomputer Center funded by Hercules foundation and Flemish government) and on the cluster system in the High Performance Computing Center (HPCC) of Nanjing University.

Software: MPI-AMRVAC (Keppens et al. 2012; Porth et al. 2014; Xia et al. 2018).

ORCID iDs

Yu-Hao Zhou https://orcid.org/0000-0002-4391-393X
C. Xia https://orcid.org/0000-0002-7153-4304
R. Keppens https://orcid.org/0000-0003-3544-2733
P. F. Chen https://orcid.org/0000-0002-7289-642X

References

Andries, J., van Doorsselaere, T., Roberts, B., et al. 2009, SSRv, 149, 3
Arregui, I., Oliver, R., & Ballester, J. L. 2012, LRSP, 9, 2
Asai, A., Ishii, T. T., Isobe, H., et al. 2012, ApJL, 745, L18
Aschwanden, M. J., Fletcher, L., Schrijver, C. J., & Alexander, D. 1999, ApJ, 520, 880
Athay, R. G., Querfeld, C. W., Smartt, R. N., Landi Degl'Innocenti, E., & Bommier, V. 1983, SoPh, 89, 3
Bashkirtsev, V. S., Kobanov, N. I., & Mashnich, G. P. 1983, SoPh, 82, 443
Bashkirtsev, V. S., & Mashnich, G. P. 1984, SoPh, 91, 93
Bocchialini, K., Baudin, F., Koutchmy, S., Pouget, G., & Solomon, J. 2011, A&A, 533, A96
Bommier, V., Landi Degl'Innocenti, E., Leroy, J.-L., & Sahal-Brechot, S. 1994, SoPh, 154, 231
Chen, J., Xie, W., Zhou, Y., et al. 2017, Ap&SS, 362, 165
Chen, P. F., Innes, D. E., & Solanki, S. K. 2008, A&A, 484, 487
Del Zanna, G., Dere, K. P., Young, P. R., Landi, E., & Mason, H. E. 2015, A&A, 582, A56
Dere, K. P., Landi, E., Mason, H. E., Monsignori Fossi, B. C., & Young, P. R. 1997, A&AS, 125, 149
Díaz, A. J., Oliver, R., & Ballester, J. L. 2002, ApJ, 580, 550
Díaz, A. J., Oliver, R., Erdélyi, R., & Ballester, J. L. 2001, A&A, 379, 1083
Díaz, A. J., & Roberts, B. 2006, SoPh, 236, 111
Dodson, H. W. 1949, ApJ, 110, 382
Eto, S., Isobe, H., Narukage, N., et al. 2002, PASJ, 54, 481
Gilbert, H. R., Daou, A. G., Young, D., Tripathi, D., & Alexander, D. 2008, ApJ, 685, 629
Gosain, S., & Foullon, C. 2012, ApJ, 761, 103
Guo, Y., Xia, C., Keppens, R., & Valori, G. 2016, ApJ, 828, 82
Hanaoka, Y., & Sakurai, T. 2017, ApJ, 851, 130
Hansteen, V. H., Archontis, V., Pereira, T. M. D., et al. 2017, ApJ, 839, 22
Hillier, A., & van Ballegooijen, A. 2013, ApJ, 766, 126
Hyder, C. L. 1966, ZAp, 63, 78
Isobe, H., & Tripathi, D. 2006, A&A, 449, L17
Jing, J., Lee, J., Spirock, T. J., et al. 2003, ApJL, 584, L103
Jing, J., Lee, J., Spirock, T. J., & Wang, H. 2006, SoPh, 236, 97
Joarder, P. S., Nakariakov, V. M., & Roberts, B. 1997, SoPh, 173, 81
Joarder, P. S., & Roberts, B. 1992, A&A, 261, 625
Joarder, P. S., & Roberts, B. 1993, A&A, 277, 225
Kaneko, T., & Yokoyama, T. 2017, ApJ, 845, 12
Keppens, R., Meliani, Z., van Marle, A. J., et al. 2012, JCoPh, 231, 718
Kleczek, J., & Kuperus, M. 1969, SoPh, 6, 72
Li, T., & Zhang, J. 2012, ApJL, 760, L10
Lin, Y. 2004, PhD thesis, Univ. Oslo
Lin, Y. 2011, SSRv, 158, 237
Luna, M., & Karpen, J. 2012, ApJL, 750, L1
Luna, M., Knizhnik, K., Muglach, K., et al. 2014, ApJ, 785, 79
Luna, M., Terradas, J., Khomenko, E., Collados, M., & de Vicente, A. 2016, ApJ, 817, 157
Mashnich, G. P., & Bashkirtsev, V. S. 2016, ARep, 60, 287
Mashnich, G. P., Bashkirtsev, V. S., & Khlystova, A. I. 2009a, Ge&Ae, 49, 891
Mashnich, G. P., Bashkirtsev, V. S., & Khlystova, A. I. 2009b, AstL, 35, 253
Merenda, L., Trujillo Bueno, J., Landi Degl'Innocenti, E., & Collados, M. 2006, ApJ, 642, 554
Nakariakov, V. M., Ofman, L., Deluca, E. E., Roberts, B., & Davila, J. M. 1999, Sci, 285, 862
Nakariakov, V. M., & Verwichte, E. 2005, LRSP, 2, 3
Ning, Z., Cao, W., Okamoto, T. J., Ichimoto, K., & Qu, Z. Q. 2009, A&A, 499, 595
Okamoto, T. J., Nakai, H., Keiyama, A., et al. 2004, ApJ, 608, 1124
Oliver, R. 2009, SSRv, 149, 175
Oliver, R., & Ballester, J. L. 1996, ApJ, 456, 393
Oliver, R., & Ballester, J. L. 2002, SoPh, 206, 45
Oliver, R., Ballester, J. L., Hood, A. W., & Priest, E. R. 1993, ApJ, 409, 809
Ouyang, Y., Zhou, Y. H., Chen, P. F., & Fang, C. 2017, ApJ, 835, 94
Pant, V., Srivastava, A. K., Banerjee, D., et al. 2015, RAA, 15, 1713
Parenti, S. 2014, LRSP, 11, 1
Porth, O., Xia, C., Hendrix, T., Moschou, S. P., & Keppens, R. 2014, ApJS, 214, 4
Ramsey, H. E., & Smith, S. F. 1966, AJ, 71, 197
Shen, Y., Liu, Y. D., Chen, P. F., & Ichimoto, K. 2014, ApJ, 795, 130
Soler, R., Oliver, R., & Ballester, J. L. 2008, ApJ, 684, 725
Soler, R., Oliver, R., & Ballester, J. L. 2010, A&A, 512, A28
Terradas, J., Oliver, R., & Ballester, J. L. 2001, A&A, 378, 635
Terradas, J., Soler, R., Díaz, A. J., Oliver, R., & Ballester, J. L. 2013, ApJ, 778, 49
Terradas, J., Soler, R., Luna, M., et al. 2016, ApJ, 820, 125
Terradas, J., Soler, R., Luna, M., Oliver, R., & Ballester, J. L. 2015, ApJ, 799, 94
Tripathi, D., Isobe, H., & Jain, R. 2009, SSRv, 149, 283
Tsubaki, T., & Takeuchi, A. 1986, SoPh, 104, 313
van Doorsselaere, T., Verwichte, E., & Terradas, J. 2009, SSRv, 149, 299
Vršnak, B., Veronig, A. M., Thalmann, J. K., & Žic, T. 2007, A&A, 471, 295
Xia, C., & Keppens, R. 2016, ApJ, 823, 22
Xia, C., Teunissen, J., El Mellah, I., Chané, E., & Keppens, R. 2018, ApJS, 234, 30
Zhang, Q. M., Chen, P. F., Xia, C., & Keppens, R. 2012, A&A, 542, A52
Zhang, Q. M., Chen, P. F., Xia, C., Keppens, R., & Ji, H. S. 2013, A&A, 554, A124
Zhang, Q. M., Li, T., Zheng, R. S., Su, Y. N., & Ji, H. S. 2017, ApJ, 842, 27
Zhou, G. P., Zhang, J., & Wang, J. X. 2016, ApJL, 823, L19
Zhou, Y.-H., Zhang, L.-Y., Ouyang, Y., Chen, P. F., & Fang, C. 2017, ApJ, 839, 9